Spatial-temporal-based Underdetermined Near-field 3-D Localization Employing a Nonuniform Cross Array

Hua Chen, *Senior Member, IEEE*, Zelong Yi, Zhiwei Jiang, Wei Liu, *Senior Member, IEEE*, Ye Tian, *Member, IEEE*, Qing Wang, *Member, IEEE* and Gang Wang, *Senior Member, IEEE*

***Abstract*—In this paper, an underdetermined three-dimensional (3-D) near-field source localization method is proposed, based on a two-dimensional (2-D) symmetric nonuniform cross array. Firstly, by utilizing the symmetric coprime array along the x-axis, a fourth-order cumulant (FOC) based matrix is constructed, followed by vectorization operation to form a single virtual snapshot, which is equivalent to the received data of a virtual array observing from virtual far-field sources, generating an increased number of degrees of freedom (DOFs) compared to the original physical array. Meanwhile, multiple delay lags, named as pseudo snapshots, are introduced to address the single snapshot issue. Then, the received data of the uniform linear array along the y-axis is similarly processed to form another virtual array, followed by a cross-correlation operation on the virtual array observations constructed from the coprime array. Finally, the 2-D angles of the near-field sources are jointly estimated by employing the recently proposed sparse and parametric approach (SPA) and the Vandermonde decomposition technique, eliminating the need for parameter discretization. To estimate the range term, the conjugate symmetry property of the signal's autocorrelation function is used to construct the second-order statistics based received data with the whole array elements, and subsequently, the one-dimensional (1-D) MUSIC algorithm is applied. Moreover, some properties of the proposed array are analyzed. Compared with existing algorithms, the proposed one has better estimation performance given the same number of sensor elements, which can work in an underdetermined and mixed sources situation, as shown by simulation results with 3-D parameters automatically paired.**

***Index Terms*—near-field, source localization, cross array, spatial-temporal, underdetermined estimation**

This work was supported by the Zhejiang Provincial Natural Science Foundation of China under Grant LY23F010003 and LR20F010001, by the National Natural Science Foundation of China under Grants 62001256, U20A20162 and 62222109, and the UK Engineering and Physical Sciences Research Council (EPSRC) under grant EP/V009419/2, and the Key Research and Development Program of Tibet Autonomous Region, and the Science and Technology Major Project of Tibetan Autonomous Region of China under grant XZ202201ZD0006G03. This paper was presented in part at IEEE International Conference on Acoustics, Speech and Signal Processing (ICASSP), 2024. For the purpose of open access, the author(s) has applied a Creative Commons Attribution (CC BY) license to any Accepted Manuscript version arising. (*Corresponding authors: Hua Chen, Ye Tian.*)

Hua Chen, Zelong Yi, Zhiwei Jiang, Ye Tian and Gang Wang are with the Faculty of Electrical Engineering and Computer Science, Ningbo University, Ningbo 315211, China. (e-mail: dkchenhua0714@hotmail.com; tianfield@126.com; wanggang@nbu.edu.cn)

Hua Chen is also with the Zhejiang Key Laboratory of Mobile Network Application Technology, Ningbo 315211, P. R. China.

Wei Liu is with the School of Electronic Engineering and Computer Science, Queen Mary University of London, London E1 4NS, UK. (e-mail: wliu.eee@gmail.com)

Qing Wang is School of Electronic Informatin Engineering, Tianjin University, Tianjin, China. (e-mail: wangq@tju.edu.cn)

I. Introduction

As an important topic in array signal processing, source localization has been applied in various fields such as radar, sonar and wireless communications [1–7]. Recently, as compared with uniform linear arrays (ULAs) [8–11], near-field (NF) source localization based on non-uniform linear arrays (NLAs) [12–21], which often have more degrees of freedom (DOF) and a larger aperture given the same number of physical elements, has attracted particular attention. However, due to the nonlinear phase difference of the near-field signal model, it is a challenging task to develop effective localization algorithms for near-field sources based on NLAs.

As a representative example, in [12], a near-field mixed-order multiple signal classification (MUSIC) localization algorithm based on sparse symmetric nested arrays is proposed, which uses the special geometry of the array to constructs a special fourth-order cumulant (FOC) matrix, and estimates the direction of arrival (DOA) of near-field signals based on the traditional MUSIC algorithm, while the range term is directly estimated from the second-order covariance matrix with the MUSIC algorithm. Using a symmetric double-nested array (SDNA), a mixed source localization method is introduced for DOA estimation with an FOC-based NF matrix followed by the spatial smoothing MUSIC (SS-MUSIC) algorithm, and the range estimates via 1-D peak searching [13]; in addition, several properties are analyzed for the SDNA. Based on a compressed symmetric nested array in [14], extended arrays are added to expand the array aperture for localization of mixed sources in [15] with optimal array configuration, leading to a high accuracy for DOA and range estimation. In [16], two nested array based sparse symmetric linear arrays (SSLAs), with closed-form sensor position expressions and an increased number of DOFs, are proposed for mixed-source localization; two FOC matrices are built for DOA and range estimation by employing spectral searching methods such as MUSIC or sparse reconstruction based ones. Treating parameter estimation of mixed sources as a regression problem, the convolution neural networks (CNN) based localization and classification method [17] is developed, exploiting the geometry of symmetric nested array, which shows improvement in estimation accuracy for both DOA and range. In [18], a symmetric displaced coprime array is designed for localization of mixed

sources, where the equivalent far-field virtual array model is constructed using the FOC, and then DOA estimation is achieved by the spatial smoothing based subspace methods or sparse reconstruction algorithms. Finally, the DOA estimate is substituted to obtain the range estimation.

In [19], a near-field parameter estimation algorithm based on symmetric ULA is proposed, which can be applied to any NLAs as long as symmetry of the array is satisfied with respect to the origin. It utilizes second-order statistics to construct equivalent far-field (FF) virtual received data, and then resorts to atomic norm minimization to transform angle estimation into a semi-positive definite programming (SDP) problem. With the estimated angle, range estimation can be achieved by a spectral peak function. A unified model for mixed sources accommodating arbitrary NLAs is proposed in [20], based on which a 2-D localization algorithm is derived with closed-form expressions for interested parameters. For partly calibrated NLAs with gain-phase uncertainties, three FOC matrices are constructed in [21] and the matrix pencil method is then applied to obtain the coarse and fine estimates of DOA and range parameters, with the array gain-phase errors calibrated at the end.

So far most of the research in this area is based on the two-dimensional (2-D) near-field source model, with rather limited attempt for the three-dimensional (3-D) case except for the method in [22], which is designed for a single source only. Although 2-D near-field algorithms can be extended to the 3-D scenario with appropriate modifications, additional matching operations are required, and furthermore, significant increase in the number of array elements may be inevitable, resulting in increased hardware costs. More importantly, it should be emphasized that existing 2-D (except for Ref. [23]) or 3-D near-field source localization methods with NLAs cannot work in the underdetermined case where the number of sources is more than that of array elements. In [23], a unified symmetric linear array framework is developed for mixed sources localization from a co-array perspective, thus resulting in increased DOFs for estimating both DOA and range of incident signals, based on a FOC matrix of the array output and covariance matrix, respectively.

In this paper, an underdetermined 3-D near-field source localization method is proposed employing a symmetric nonuniform cross array. We first exploit the FOC of the near-field observations with multiple delay lags to construct virtual far-field pseudo-observations, providing increased DOFs. Then, the recently proposed sparse and parametric approach (SPA) [24] and Vandermonde decomposition technique [25] are employed to jointly estimate the 2-D angles of the near-field sources, eliminating the need for parameter discretization. Finally, by resorting to conjugate symmetry property of the signal's autocorrelation function, the one-dimensional (1-D) MUSIC algorithm is applied to the extended data for range estimation.

Notations: Matrices and vectors are denoted by boldfaced uppercase and lowercase letters, respectively. The superscripts $(\cdot)^T$, $(\cdot)^*$, $(\cdot)^H$ stand for transpose, conjugate and conjugate transpose, respectively. The notations $E\{\cdot\}$, $\otimes$ and $\odot$ represent the statistical expectation, Kronecker product, Khatri-Rao (KR) product, respectively. $diag\{\mathbf{Z}\}$ gives diagonal elements of the matrix $\mathbf{Z}$. $tr(\cdot)$ and $vec(\cdot)$ denote the trace and vectorization operation, respectively.

II. Signal Model

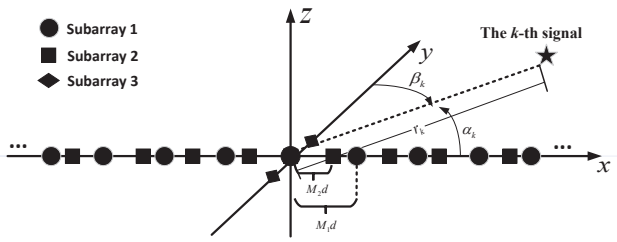

Fig. 1. 3-D localization configuration for NF sources with a symmetric nonuniform cross array.

As shown in Fig.1, the considered array consists of three sub-ULAs symmetric about the origin and have a common element located at the origin. Subarray 1 and subarray 2 form a coprime array and are both located on the x-axis, with coprime numbers M_1 and M_2 being the number of elements on each side of the origin, respectively. The whole set of array element positions on the x-axis is denoted as $\mathbb{S}_x$. Subarray 3 is located on the y-axis and consists of M_y elements. Similarly, the set of element positions on the y-axis is denoted as $\mathbb{S}_y$. The element spacing of the three subarrays is M_2d, M_1d and d, respectively, where $d = \lambda/4$ with λ being the signal wavelength. Assume that there are K spatially and temporally uncorrelated NF narrowband sources incident on the array. The 2-D angles of the kth source with respect to the x-axis and y-axis are represented as α_k and β_k, respectively, and the range with respect to the origin is represented as r_k. Thus, the kth source can be characterized by a parameter pair (α_k, β_k, r_k). At time instant t, the received data from the three subarrays can be respectively represented as

$$\mathbf{x}_1(t) = \mathbf{A}_1(\alpha, r)\mathbf{s}(t) + \mathbf{n}_1(t), \tag{1}$$

$$\mathbf{x}_2(t) = \mathbf{A}_2(\alpha, r)\mathbf{s}(t) + \mathbf{n}_2(t), \tag{2}$$

$$\mathbf{y}(t) = \mathbf{A}_y(\beta, r)\mathbf{s}(t) + \mathbf{n}_y(t), \tag{3}$$

where $\mathbf{A}_1(\alpha, r) = [\mathbf{a}_1(\alpha_1, r_1), \mathbf{a}_1(\alpha_2, r_2), \cdots, \mathbf{a}_1(\alpha_K, r_K)] \in \mathbb{C}^{(2M_1-1)\times K}$, $\mathbf{A}_2(\alpha, r) = [\mathbf{a}_2(\alpha_1, r_1), \mathbf{a}_2(\alpha_2, r_2), \cdots, \mathbf{a}_2(\alpha_K, r_K)] \in \mathbb{C}^{(2M_2-1)\times K}$, $\mathbf{A}_y(\alpha, r) = [\mathbf{a}_y(\beta_1, r_1), \mathbf{a}_y(\beta_2, r_2), \cdots, \mathbf{a}_y(\beta_K, r_K)] \in \mathbb{C}^{M_y\times K}$ are the steering matrices of the three subarrays with each element in the corresponding column being $\mathbf{a}_{1m}(\alpha_k, r_k) = e^{-j\tau_{1m,k}}$, $\mathbf{a}_{2m'}(\alpha_k, r_k) = e^{-j\tau_{2m',k}}$ and $\mathbf{a}_{yn}(\beta_k, r_k) = e^{-j\tau_{yn,k}}$, respectively, where $-(M_1 - 1) \leqslant m \leqslant (M_1 - 1)$, $-(M_2 - 1) \leqslant m' \leqslant (M_2 - 1)$, $-(M_y - 1)/2 \leqslant n \leqslant (M_y - 1)/2$, and $\tau_{1m,k}$, $\tau_{2m',k}$, and $\tau_{yn,k}$ represent the propagation delays of the kth source from the 0th to the mth and the m'th sensors of subarray 1 and subarray 2, and the nth sensor of subarray 3, respectively. $\mathbf{s}(t) = [s_1(t), s_2(t), \cdots, s_K(t)]$ is the incident signal vector, and $\mathbf{n}_1(t)$, $\mathbf{n}_2(t)$, and $\mathbf{n}_y(t)$ are the corresponding additive white Gaussian noise vectors. For convenience, in the following, the steering matrices of the three subarrays are simplified

into $\mathbf{A}_1$, $\mathbf{A}_2$, and $\mathbf{A}_y$, respectively. Considering the k-th column of $\mathbf{A}_1$, $\mathbf{A}_2$ and $\mathbf{A}_y$, which is also referred to as steering vectors, with the Fresnel approximation [26–28], we have

$$\begin{aligned}\mathbf{a}_1(\alpha_k, r_k) =&[e^{-j[-(M_1-1)M_2 w_{xk}+(-M_1+1)^2 M_2^2 \varphi_{xk}]},\\ &e^{-j[-(M_1-2)M_2 w_{xk}+(-M_1+2)^2 M_2^2 \varphi_{xk}]},\\ &\cdots, e^{-j[(M_1-1)M_2 w_{xk}+(M_1-1)^2 M_2^2 \varphi_{xk}]}]^T,\end{aligned} \tag{4}$$

$$\begin{aligned}\mathbf{a}_2(\alpha_k, r_k) =&[e^{-j[-(M_2-1)M_1 w_{xk}+(-M_2+1)^2 M_1^2 \varphi_{xk}]},\\ &e^{-j[-(M_2-2)M_1 w_{xk}+(-M_2+2)^2 M_1^2 \varphi_{xk}]},\\ &\cdots, e^{-j[(M_2-1)M_1 w_{xk}+(M_2-1)^2 M_1^2 \varphi_{xk}]}]^T,\end{aligned} \tag{5}$$

$$\begin{aligned}\mathbf{a}_y(\beta_k, r_k) =&[e^{-j[-((M_y-1)/2) w_{yk}+(-(M_y-1)/2)^2 \varphi_{yk}]}, \cdots,\\ &1, \cdots, e^{-j[((M_y-1)/2) w_{yk}+((M_y-1)/2)^2 \varphi_{yk}]}]^T,\end{aligned} \tag{6}$$

where $w_{xk} = -2\pi d\cos(\alpha_k)/\lambda$, $\varphi_{xk} = \pi d^2 \sin^2(\alpha_k)/\lambda r_k$, $w_{yk} = -2\pi d\cos(\beta_k)/\lambda$, and $\varphi_{yk} = \pi d^2 \sin^2(\beta_k)/\lambda r_k$.

Overall, we use $\mathbf{x}(t)$ to represent the array output of the entire x-axis and $\mathbf{z}(t)$ the output of the entire physical array, expressed as,

$$\begin{aligned}\mathbf{x}(t) = \begin{bmatrix}\mathbf{x}_1(t)\\ \mathbf{x}_2(t)\end{bmatrix} &= \begin{bmatrix}\mathbf{A}_1\\ \mathbf{A}_2\end{bmatrix}\mathbf{s}(t) + \begin{bmatrix}\mathbf{n}_1(t)\\ \mathbf{n}_2(t)\end{bmatrix}\\ &= \mathbf{A}_x\mathbf{s}(t) + \mathbf{n}_x(t),\end{aligned} \tag{7}$$

$$\begin{aligned}\mathbf{z}(t) = \begin{bmatrix}\mathbf{x}(t)\\ \mathbf{y}(t)\end{bmatrix} &= \begin{bmatrix}\mathbf{A}_x\\ \mathbf{A}_y\end{bmatrix}\mathbf{s}(t) + \begin{bmatrix}\mathbf{n}_x(t)\\ \mathbf{n}_y(t)\end{bmatrix}\\ &= \mathbf{A}_z\mathbf{s}(t) + \mathbf{n}_z(t).\end{aligned} \tag{8}$$

III. The Proposed Algorithm

In this section, by jointly exploiting the spatial and temporal information of incident signals, the FOC of array observations is utilized to construct the virtual array data equivalent to the far-field (FF) pseudo observations, which increases the DOFs compared to the original physical array. The specific construction method for the virtual FF pseudo observations is provided as follows.

A. Construction of virtual FF data

At first, by appropriately selecting elements of the subarrays along the x-axis, the FOC of the array output at lag τ is calculated as follows

$$\begin{aligned}\mathbf{C}_1(p,q,\tau) &= cum\{\mathbf{x}(p, t+\tau), \mathbf{x}^*(-p, t),\\ &\quad \mathbf{x}(-q, t+\tau), \mathbf{x}^*(q, t)\}\\ &= \sum_{k=1}^{K} e^{-j[2(p-q)w_{xk}]}\\ &\quad cum\left\{s_k(t+\tau), s_k^*(t), s_k(t+\tau), s_k^*(t)\right\}\\ &= \sum_{k=1}^{K} e^{-j2(p-q)w_{xk}} c_{sk}(\tau),\end{aligned} \tag{9}$$

where $p, q \in \mathbb{S}_x$, $\mathbf{x}(p,t)$ represents the received data at position p on the x-axis array at time t, and $c_{sk}(\tau) = cum\{s_k(t+\tau), s_k^*(t), s_k(t+\tau), s_k^*(t)\}$, is the FOC of the k-th signal at lag τ. For each τ, vectorizing $\mathbf{C}_1$ yields

$$\mathbf{c}_1(\tau) = vec(\mathbf{C}_1(:,:,\tau)) = \mathbf{B}_1\mathbf{c}_s(\tau), \tag{10}$$

where $\mathbf{c}_s(\tau) = [c_{s1}(\tau), c_{s2}(\tau), \cdots, c_{sK}(\tau)]^T$ is the FOC vector for the signal at lag τ. Here, $\mathbf{c}_1(\tau)$ can be considered as the virtual data of FF sources, while $\mathbf{B}_1$ the corresponding steering matrix.

It is evident that positions of virtual array elements are the sum and difference set between the positions of array elements in subarray 1 and subarray 2. As pointed out in [29], there exist some redundant elements in the coprime array, and thus by removing the redundancy from $\mathbf{c}_1(\tau)$, the new virtual array received data can be expressed as

$$\tilde{\mathbf{c}}_1(\tau) = \tilde{\mathbf{B}}_1\mathbf{c}_s(\tau), \tag{11}$$

where $\tilde{\mathbf{B}}_1$ is the new virtual array steering matrix. By uniformly sampling the lag τ, L pseudo snapshots are collected for the virtual received data as

$$\tilde{\mathbf{C}}_1 = [\tilde{\mathbf{c}}_1(T_s), \tilde{\mathbf{c}}_1(2T_s), \cdots, \tilde{\mathbf{c}}_1(LT_s)] = \tilde{\mathbf{B}}_1\mathbf{C}_s, \tag{12}$$

where $\mathbf{C}_s = [\mathbf{c}_s(T_s), \mathbf{c}_s(2T_s), \cdots, \mathbf{c}_s(LT_s)]$. Compared to the original received data, the number of virtual array elements corresponding to the constructed virtual FF data is greatly increased. Furthermore, with the usage of FOC, the range term is eliminated, which conveniently allows subsequent 2-D angle estimation.

B. Estimate α_k and β_k

In order to avoid the off-grid problem in existing sparse reconstruction based methods, the matrix reconstruction technique called SPA is used to recover a covariance matrix with Toeplitz structure. However, due to the possibility of holes in the above virtual FF received data, as proven in Sec. IV, its noise-free covariance matrix may not be Toeplitz. Therefore, directly using the virtual received data for covariance matrix recovery requiring a Toeplitz structure may lead to a failure. Fortunately, it can be proved that the virtual array is definitely a redundant array (detailed proof can be found in Sec. IV), whose co-array is equivalent to a corresponding ULA with the same array aperture.

To proceed, denote $\mathbf{B}_\Sigma$ as the co-array manifold matrix of the virtual array observing FF sources, which has a Vandermonde structure. Given a selection matrix $\mathbf{\Gamma}$, the relationship between $\tilde{\mathbf{B}}_1$ and $\mathbf{B}_\Sigma$ can be expressed as follows

$$\tilde{\mathbf{B}}_1 = \mathbf{\Gamma}\mathbf{B}_\Sigma, \tag{13}$$

where $\mathbf{\Gamma}$ is a $P \times Q$ matrix, P is the number of elements in the virtual array, and Q is the number of elements in the corresponding co-array.

Therefore, by calculating the covariance matrix of $\tilde{\mathbf{C}}_1$ with the help of (13), we have

$$\begin{aligned}\mathbf{R}_1 &= E\left\{\tilde{\mathbf{C}}_1\tilde{\mathbf{C}}_1^H\right\}\\ &= \tilde{\mathbf{B}}_1\mathbf{C}_s\mathbf{C}_s^H\tilde{\mathbf{B}}_1^H\\ &= \tilde{\mathbf{B}}_1\mathbf{P}\tilde{\mathbf{B}}_1^H\\ &= \mathbf{\Gamma}\mathbf{B}_\Sigma\mathbf{P}\mathbf{B}_\Sigma^H\mathbf{\Gamma}^H,\end{aligned} \tag{14}$$

where $\mathbf{P}$ is a diagonal matrix with all its diagonal elements being non-negative. Define $\mathbf{R}_\Sigma = \mathbf{B}_\Sigma \mathbf{P} \mathbf{B}_\Sigma^H$, and since $\mathbf{B}_\Sigma$ is a Vandermonde matrix, $\mathbf{R}_\Sigma$ is Toeplitz. Although $\mathbf{R}_1$ may not necessarily be a Toeplitz matrix, it encompasses all the elements present in $\mathbf{R}_\Sigma$ by introducing an appropriate selection matrix $\mathbf{\Gamma}$ for the symmetric coprime array.

In order to estimate 2-D angles simultaneously, we further utilize the received data from subarray 3 to construct another virtual array received data, i.e.,

$$\begin{aligned}\mathbf{C}_2(u,v,\tau) &= cum\{\mathbf{y}(u,t+\tau), \mathbf{y}^*(-u,t), \\ &\quad \mathbf{y}(-v,t+\tau), \mathbf{y}^*(v,t)\} \\ &= \sum_{k=1}^{K} e^{-j2(u-v)w_{yk}} c_{sk}(\tau),\end{aligned} \tag{15}$$

where $u, v \in \{-(M_y-1)/2, \cdots, 0, \cdots, (M_y-1)/2\}$.

Expressing (15) in a matrix form, and then applying vectorization together with redundancy-removal operations, we have

$$\mathbf{c}_2(\tau) = \mathbf{B}_2 \mathbf{c}_s(\tau), \tag{16}$$

where $\mathbf{B}_2 = [\mathbf{b}_{21}, \mathbf{b}_{22}, \cdots, \mathbf{b}_{2K}]$ is the virtual array manifold matrix constructed by subarray 3, and $\mathbf{b}_{2k} = [e^{-j2(-(M_y-1))w_{yk}}, e^{-j2(-(M_y-2))w_{yk}}, \cdots, e^{-j2(M_y-1)w_{yk}}]$ denotes the steering vector corresponding to the kth column of $\mathbf{B}_2$. Similar to (12), L pseudo snapshots of the virtual received data can be obtained as

$$\mathbf{C}_2 = [\mathbf{c}_2(T_s), \mathbf{c}_2(2T_s), \cdots, \mathbf{c}_2(LT_s)] = \mathbf{B}_2 \mathbf{C}_s, \tag{17}$$

where the manifold matrix $\mathbf{B}_2$ of the virtual received data $\mathbf{C}_2$ is of Vandermonde form, and thus its covariance matrix possesses a Toeplitz structure. Then, to construct a two-level Toeplitz matrix by performing cross-correlation and vectorization operations on $\tilde{\mathbf{C}}_1$ and $\mathbf{C}_2$, one can obtain

$$\mathbf{r}_1 = vec(E\{\mathbf{C}_2 \tilde{\mathbf{C}}_1^H\}) = (\tilde{\mathbf{B}}_1^* \odot \mathbf{B}_2)\mathbf{r}_{cs} = \mathbf{D}_1 \mathbf{r}_{cs}, \tag{18}$$

where $\mathbf{r}_{cs}$ is a vector formed by the diagonal elements of the covariance matrix of $\mathbf{C}_s$. Since $\tilde{\mathbf{B}}_1^*$ may not necessarily be a Vandermonde matrix, $\mathbf{D}_1$ may not possess a two-level Vandermonde structure. Therefore, substitute (13) to (18), leading to

$$\begin{aligned}\mathbf{r}_1 &= (\tilde{\mathbf{B}}_1^* \odot \mathbf{B}_2)\mathbf{r}_{cs} \\ &= (\mathbf{\Gamma}\mathbf{B}_\Sigma^* \odot \mathbf{B}_2)\mathbf{r}_{cs} \\ &= [\mathbf{\Gamma}\mathbf{b}_{\Sigma 1}^* \otimes \mathbf{b}_{21}, \cdots, \mathbf{\Gamma}\mathbf{b}_{\Sigma K}^* \otimes \mathbf{b}_{2K}]\mathbf{r}_{cs} \\ &= [\mathbf{\Gamma}\mathbf{b}_{\Sigma 1}^* \otimes \mathbf{I}_{(2M_y-1)\times(2M_y-1)}\mathbf{b}_{21}, \cdots, \mathbf{\Gamma}\mathbf{b}_{\Sigma K}^* \otimes \\ &\quad \mathbf{I}_{(2M_y-1)\times(2M_y-1)}\mathbf{b}_{2K}]\mathbf{r}_{cs} \\ &= [(\mathbf{\Gamma} \otimes \mathbf{I}_{(2M_y-1)\times(2M_y-1)})(\mathbf{b}_{\Sigma 1}^* \otimes \mathbf{b}_{21}), \cdots, \\ &\quad (\mathbf{\Gamma} \otimes \mathbf{I}_{(2M_y-1)\times(2M_y-1)})(\mathbf{b}_{\Sigma K}^* \otimes \mathbf{b}_{2K})]\mathbf{r}_{cs} \\ &= (\mathbf{\Gamma} \otimes \mathbf{I}_{(2M_y-1)\times(2M_y-1)})(\mathbf{B}_\Sigma^* \odot \mathbf{B}_2)\mathbf{r}_{cs} \\ &= \mathbf{\Gamma}_\Sigma(\mathbf{B}_\Sigma^* \odot \mathbf{B}_2)\mathbf{r}_{cs},\end{aligned} \tag{19}$$

where $\mathbf{I}_{(2M_y-1)\times(2M_y-1)}$ is an identity matrix, $\mathbf{\Gamma}_\Sigma = (\mathbf{\Gamma} \otimes \mathbf{I}_{(2M_y-1)\times(2M_y-1)})$ is a selection matrix, and $\mathbf{b}_{\Sigma k}$ represents the kth column of $\mathbf{B}_\Sigma$. The covariance matrix of $\mathbf{r}_1$ can be calculated as follows

$$\mathbf{R_2} = E\{\mathbf{r}_1 \mathbf{r}_1^H\} = \mathbf{\Gamma}_\Sigma \mathbf{T}_\Sigma \mathbf{\Gamma}_\Sigma^H, \tag{20}$$

where $\mathbf{T}_\Sigma = (\mathbf{B}_\Sigma^* \odot \mathbf{B}_2)\mathbf{r}_{cs}\mathbf{r}_{cs}^H(\mathbf{B}_\Sigma^* \odot \mathbf{B}_2)^H$ is a two-level Toeplitz matrix. Similar to (14) for the non-Toeplitz case, although $\mathbf{R_2}$ may not be a two-level Toeplitz matrix, it contains all the elements of the two-level Toeplitz matrix $\mathbf{T}_\Sigma$, which is used for 2-D angle estimation.

In practice, as the number of snapshots is limited, the FOC-based covariance matrix $\mathbf{R_2}$ is obtained through maximum likelihood estimation using the sample data. Then, matrix recovery techniques are required to recover the Toeplitz form of the matrix $\mathbf{T}_\Sigma$. Here, the SPA [24], which could carry out parameter estimation in the continuous range without discretization, is utilized to recover the corresponding noiseless matrix of $\mathbf{T}_\Sigma$. The optimization is formulated as follows

$$\begin{aligned}&\min_{\mathbf{w}, \mathbf{T}_\Sigma} ||\mathbf{r}_1||_2^2 \mathbf{w} + tr[\mathbf{T}_\Sigma] \\ &s.t. \begin{bmatrix} \mathbf{w} & \mathbf{r}_1^H \\ \mathbf{r}_1 & \mathbf{T}_\Sigma \end{bmatrix} \succcurlyeq 0 \ .\end{aligned} \tag{21}$$

After $\mathbf{T}_\Sigma$ is obtained by using the SDP solver, the Vandermonde decomposition technique called matrix pencil and pairing (MaPP) [25] is applied for the two-level Toeplitz matrix $\mathbf{T}_\Sigma$ to obtain the estimates for the automatically paired angles $\hat{\alpha}$ and $\hat{\beta}$. The theorem of MaPP is restated below.

Theorem 1 ([25]): Given a positive semi-definite two-level Toeplitz matrix $\mathbf{T}_\Sigma$ with $rank(\mathbf{T}_\Sigma) < min\{M_x, M_y\}$, where M_x and M_y denote the total number of array elements on x-axis and y-axis, respectively, $\mathbf{T}_\Sigma$ can be uniquely decomposed as

$$\mathbf{T}_\Sigma = \sum_{k=1}^{K} p_k(\mathbf{a}_x(-\alpha_k)\mathbf{a}_x^H(-\alpha_k)) \otimes (\mathbf{a}_y(\beta_k)\mathbf{a}_y^H(\beta_k)), \tag{22}$$

where $p_k > 0$.

Remark 1: It should be noted that, although the above theorem is valid when $rank(\mathbf{T}_\Sigma) < min\{M_x, M_y\}$, it is shown in [25] that when $rank(\mathbf{T}_\Sigma) \geqslant min\{M_x, M_y\}$, the correct decomposition can also be found with large probability.

C. Estimate r_k

In this part, the range parameters are estimated by fully utilizing the spatial-temporal information of the signals, which also works in underdetermined scenarios. Applying the cross-correlation operation to the observation of each physical element and that of the origin element, one can have

$$\mathbf{r}_z(\tau) = E\left\{\mathbf{z}(t+\tau) z_0^H(t)\right\} = \mathbf{A}_z \mathbf{r}_s(\tau), \tag{23}$$

$$\mathbf{r}_z(-\tau) = E\left\{\mathbf{z}(t) z_0^H(t+\tau)\right\} = \mathbf{A}_z \mathbf{r}_s(-\tau), \tag{24}$$

where $z_0(t)$ represents the observation at the origin element at time t, and $\mathbf{r}_s(\tau) = diag\left\{E\left\{\mathbf{s}(t+\tau)\mathbf{s}^H(t)\right\}\right\}$. Since $\mathbf{r}_s(\tau) = \mathbf{r}_s^*(-\tau)$, we obtain

$$\mathbf{r}_z^*(-\tau) = (\mathbf{A}_z \mathbf{r}_s(-\tau))^* = \mathbf{A}_z^* \mathbf{r}_s^*(-\tau) = \mathbf{A}_z^* \mathbf{r}_s(\tau). \tag{25}$$

Then, cascading $\mathbf{r}_z(\tau)$ and $\mathbf{r}_z^*(-\tau)$ by column, a new column is constructed as follows

$$\tilde{\mathbf{r}}_z(\tau) = \begin{bmatrix} \mathbf{r}_z(\tau) \\ \mathbf{r}_z^*(-\tau) \end{bmatrix} = \begin{bmatrix} \mathbf{A}_z \\ \mathbf{A}_z^* \end{bmatrix} \mathbf{r}_s(\tau) = \tilde{\mathbf{A}}_z \mathbf{r}_s(\tau). \tag{26}$$

Similar to (12), by uniformly sampling lag τ, the L pseudo snapshots data matrix $\tilde{\mathbf{R}}_z(\tau)$ is obtained as

$$\tilde{\mathbf{R}}_z = [\tilde{\mathbf{r}}_z(T_s), \tilde{\mathbf{r}}_z(2T_s), \cdots, \tilde{\mathbf{r}}_z(LT_s)] = \tilde{\mathbf{A}}_z \mathbf{R}_s, \tag{27}$$

where $\mathbf{R}_s = [\mathbf{r}_s(T_s), \mathbf{r}_s(2T_s), \cdots, \mathbf{r}_s(LT_s)]$. By applying the 1-D MUSIC algorithm to $\tilde{\mathbf{R}}_z$ and then conducting 1-D peak search related to the range parameter by substituting the estimated 2-D angles, estimation of the range parameters is then achieved.

The proposed algorithm is summarized as follows.

Proposed Algorithm

Input: T snapshots of array observations $\mathbf{x}(t)$ and $\mathbf{y}(t)$ $(t = 1, \cdots, T)$.

Output: 3-D parameters (α_k, β_k and r_k) of the k-th NF signal.

1. Construct virtual FF observation of $\mathbf{C}_1$ on x-axis by exploiting the FOC.
2. Vectorize on virtual array observation and then remove the redundancy to get $\tilde{\mathbf{C}}_1$ with L pseudo snapshots.
3. Apply a similar process on y-axis to obtain $\mathbf{C}_2$.
4. Perform cross-correlation operation on $\tilde{\mathbf{C}}_1$ and $\mathbf{C}_2$ to obtain single snapshot data $\mathbf{r}_1$.
5. Apply SPA and MaPP on $\mathbf{r}_1$ to estimate α_k and β_k.
6. Construct the second-order statistics $\tilde{\mathbf{R}}_z$ and apply 1-D MUSIC to estimate r_k.

IV. Analysis of the Properties of the Proposed Array

As shown in Fig. 1, the position set of the symmetric co-prime array in x-axis can be represented as

$$\begin{aligned}\mathbb{S}_x =& \{m_1 M_2 d, -(M_1-1) \leqslant m_1 \leqslant (M_1-1)\} \cup \\ & \{m_2 M_1 d, -(M_2-1) \leqslant m_2 \leqslant (M_2-1)\},\end{aligned} \tag{28}$$

where according to (9), the position set of the corresponding virtual array can be obtained as

$$\mathbb{V} = \{u_i - u_j | u_i, u_j \in \mathbb{S}_x, i, j = 1, 2, \cdots, 2(M_1+M_2)-3\}. \tag{29}$$

Obviously, the element positions set in (29) is the difference co-array (DCA) set of the physical element positions, which can be divided into two parts: one part is the FOC-based self-DCA sets, denoted as $\mathbb{L}_{s1}$ and $\mathbb{L}_{s2}$, of subarray 1 and subarray 2 respectively, and the other part is the FOC-based cross-DCA set $\mathbb{L}_c$ between the above two subarrays. Thus, $\mathbb{V}$ can be rewritten as the union of the three subsets as follows

$$\mathbb{V} = \mathbb{L}_{s1} \cup \mathbb{L}_{s2} \cup \mathbb{L}_c, \tag{30}$$

where $\mathbb{L}_{s1} = \{\ell_{s1} | \ell_{s1} = (k_1 - k_2) M_2 d, -(M_1-1) \leqslant k_1, k_2 \leqslant (M_1-1)\}$, $\mathbb{L}_{s2} = \{\ell_{s2} | \ell_{s2} = (k_1 - k_2) M_1 d, -(M_2-1) \leqslant k_1, k_2 \leqslant (M_2-1)\}$, $\mathbb{L}_c = \{\ell_c | \ell_c = (k_1 M_2 - k_2 M_1) d, |k_1| \leqslant (M_1-1), |k_2| \leqslant (M_2-1)\}$.

The subsets $\mathbb{L}_{s1}$ and $\mathbb{L}_{s2}$ can be equivalently represented as

$$\mathbb{L}_{s1} = \{\ell_{s1} | \ell_{s1} = m M_2 d, -2(M_1-1) \leqslant m \leqslant 2(M_1-1)\}, \tag{31}$$

$$\mathbb{L}_{s2} = \{\ell_{s2} | \ell_{s2} = n M_1 d, -2(M_2-1) \leqslant n \leqslant 2(M_2-1)\}. \tag{32}$$

It can be seen from (31) and (32) that the virtual array aperture of the two subarrays is twice that of the physical subarrays, but there are holes in the co-array set united $\mathbb{L}_{s1}$ with $\mathbb{L}_{s2}$, and the subset $\mathbb{L}_c$ also should be considered.

A. The properties and related proof of $\mathbb{L}_c$

Proposition 1:

a) $\mathbb{L}_c$ is symmetric about the origin.

Proof: Assume that $0 \leqslant k_1 \leqslant (M_1-1)$, $-(M_2-1) \leqslant k_2 \leqslant (M_2-1)$, we have:

$$\ell'_{c1} = k_1 M_2 - k_2 M_1. \tag{33}$$

Then, when $-(M_1-1) \leqslant k_3 \leqslant 0$, let $k_4 = -k_2$, and we obtain

$$\begin{aligned}\ell'_{c2} &= k_3 M_2 - k_4 M_1 \\ &= -k_1 M_2 - k_4 M_1 \\ &= -k_1 M_2 - (-k_2 M_1) \\ &= k_2 M_1 - k_1 M_2.\end{aligned} \tag{34}$$

It can be seen from (33) and (34) that the values of the sets ℓ'_{c1} and ℓ'_{c2} are symmetric about the origin, so $\mathbb{L}_c$ is symmetric about the origin.

b) The number of different elements of $\mathbb{L}_c$ is $(2M_1-1)(2M_2-1) - (M_1-1)(M_2-1)$.

Proof: Define k_1, k_2, k_3 and k_4, which satisfy $-(M_1-1) \leqslant k_1, k_3 \leqslant (M_1-1)$, $-(M_2-1) \leqslant k_2, k_4 \leqslant (M_2-1)$, $k_1 \neq k_3$, $k_2 \neq k_4$. Assume that $k_1 M_2 - k_2 M_1 = k_3 M_2 - k_4 M_1$, and we can get

$$\frac{M_1}{M_2} = \frac{k_1 - k_3}{k_2 - k_4}. \tag{35}$$

With the range of values for k_1, k_2, k_3 and k_4, one can easily obtain that $-2(M_1-1) \leqslant k_1 - k_3 \leqslant 2(M_1-1)$, $-2(M_2-1) \leqslant k_2 - k_4 \leqslant 2(M_2-1)$. Since M_1 and M_2 are co-prime, (35) holds only if the following equations are satisfied,

$$k_1 - k_3 = M_1, k_2 - k_4 = M_2, \tag{36}$$

$$k_1 - k_3 = -M_1, k_2 - k_4 = -M_2. \tag{37}$$

The values of each parameter that satisfy (36) are $1 \leqslant k_1 \leqslant M_1-1$, $k_3 = k_1 - M_1$, $1 \leqslant k_2 \leqslant M_2-1$, $k_4 = k_2 - M_2$, where there are a total of $(M_1-1)(M_2-1)$ combinations. Furthermore, it is easy to know that the combinations satisfying (37) are the same as (36). Obviously, the total number of elements (including duplicate elements) in $\mathbb{L}_c$ is $(2M_1-1)(2M_2-1)$, and by removing duplicate elements, the number of different elements is $(2M_1-1)(2M_2-1) - (M_1-1)(M_2-1)$.

c) $\mathbb{L}_c$ contains all integer multiples of d in the range of $-(M_1M_2-1)d \leqslant \ell_c \leqslant (M_1M_2-1)d$.

Proof: The above sub-proposition can be transformed into another formulation: given any integer $\ell_c \in [-(M_1M_2-1), M_1M_2-1]$, we can find $-(M_1-1) \leqslant k_1 \leqslant (M_1-1)$, $-(M_2-1) \leqslant k_2 \leqslant (M_2-1)$, satisfying $\ell_c = k_1 M_2 - k_2 M_1$.

As proven earlier, the range of ℓ_c is symmetric about the origin, so one has only to prove that given any integer $\ell'_{c1} \in [0, M_1M_2-1]$, we can find $0 \leqslant k_1 \leqslant (M_1-1)$, $-(M_2-1) \leqslant k_2 \leqslant (M_2-1)$, satisfying $\ell'_{c1} = k_1 M_2 - k_2 M_1$. Rewrite $\ell'_{c1} = k_1 M_2 - k_2 M_1$ as follows

$$k_2 M_1 = k_1 M_2 - \ell_{c1}, \tag{38}$$

and substituting $0 \leqslant k_1 \leqslant (M_1-1)$ and $\ell'_{c1} \in [0, M_1M_2-1]$ into (38), we have $-(M_1M_2-1) \leqslant k_2 M_1 \leqslant (M_1-1)M_2$,

and further infer that $-M_1M_2 < k_2M_1 < M_1M_2$, finally get $-M_2 < k_2 < M_2$.

d) $-[2M_1M_2-(M_1+M_2)]\,d \leqslant \ell_c \leqslant [2M_1M_2-(M_1+M_2)]\,d$ **is the element range of** $\mathbb{L}_c$.

Proof: When $k_1 = -(M_1-1), k_2 = M_2-1$, ℓ_c provides the minimum value of $-[2M_1M_2-(M_1+M_2)]$. When $k_1 = M_1-1, k_2 = -(M_2-1)$, ℓ_c reaches the maximum value of $2M_1M_2-(M_1+M_2)$.

e) In the positive half of $\mathbb{L}_c$**,** $M_1M_2+aM_1+bM_2, a \geqslant 0, b \geqslant 0$ **is the hole position.**

Proof: Assume that $\ell_c = k_1M_2-k_2M_1 = M_1M_2+aM_1+bM_2$, $a \geqslant 0$, $b \geqslant 0$, $-(M_1-1) \leqslant k_1 \leqslant (M_1-1)$, $-(M_2-1) \leqslant k_2 \leqslant (M_2-1)$, we can get

$$\frac{M_1}{M_2} = \frac{k_1-b}{M_2+k_2+a}. \tag{39}$$

Since $k_1-b \leqslant M_1-1$, $M_2+k_2+a \geqslant 1$ and M_1, M_2 are co-prime, (39) does not hold, and in turn, we get the hole position in $\mathbb{L}_c$.

B. The properties and related proof of $\mathbb{V}$

Proposition 2:

a) The minimum continuous element position range of $\mathbb{V}$ **is** $[-M_1M_2d, M_1M_2d]$.

Proof: Since $\mathbb{L}_{s1}$ and $\mathbb{L}_{s2}$ contain elements $-M_1M_2d$ and M_1M_2d, respectively, and combined with Proposition 1-c, it can be seen that the continuous element position range of $\mathbb{V}$ is $[-M_1M_2d, M_1M_2d]$.

b) The total number of elements in $\mathbb{V}$ **is** $3M_1M_2+(M_1+M_2)-6$.

Proof: According to Proposition 1-c, we know that the subset of $\mathbb{L}_{s1}$ and $\mathbb{L}_{s2}$ within the range of $[-(M_1M_2-1)d, (M_1M_2-1)d]$ is a subset of $\mathbb{L}_c$. Then, assuming that $\mathbb{L}_{s1}$ and $\mathbb{L}_{s2}$ have the same elements as $\mathbb{L}_c$ within the range of $((M_1M_2-1)d, \max\{2(M_1-1)M_2d, 2(M_2-1)M_1d\}]$, the following results can be obtained

$$\begin{aligned} mM_2 &= k_1M_2-k_2M_1, M_1 \leqslant m \leqslant 2(M_1-1) \\ nM_1 &= k_3M_2-k_4M_1, M_2 \leqslant n \leqslant 2(M_2-1). \end{aligned} \tag{40}$$

By simply transforming the above equation, we obtain

$$\begin{aligned} \frac{M_1}{M_2} &= \frac{k_1-m}{k_2} \\ \frac{M_1}{M_2} &= \frac{k_3}{k_4-n}. \end{aligned} \tag{41}$$

Since $-(M_1-1) \leqslant k_1, k_3 \leqslant (M_1-1)$ and $-(M_2-1) \leqslant k_2, k_4 \leqslant (M_2-1)$, it is easy to obtain that $k_1-m < 0, k_2 \geqslant -(M_2-1), k_3 \geqslant -(M_1-1), k_4-n < 0$. Recall that M_1 and M_2 are co-prime, and thus, (41) does not hold, according to which, we can infer that $\mathbb{L}_{s1}$ and $\mathbb{L}_{s2}$ do not have the same elements as $\mathbb{L}_c$ in the range of $((M_1M_2-1)d, \max\{2(M_1-1)M_2d, 2(M_2-1)M_1d\}]$.

Above all, the total number of non-redundant elements in the virtual array is given as follows

$$\begin{aligned} &\underbrace{(2M_1-1)(2M_2-1)-(M_1-1)(M_2-1)}_{\text{cross-DCA}} \\ &+\underbrace{2(M_1-1)+2(M_2-1)-2}_{\text{self-DCA}} \\ &= 3M_1M_2+(M_1+M_2)-6. \end{aligned} \tag{42}$$

Proposition 3: *The Virtual array* $\mathbb{V}$ *is a redundant array.*

Proof: The proof of proposition 3 can be converted to prove that the co-array of the virtual array $\mathbb{V}$ is equivalent to a ULA with the same array aperture. First, we give the co-array set of $\mathbb{V}$ as follows

$$\mathbf{\Sigma}_V = \{\ell_V | \ell_V = m_1-m_2+1, m_1, m_2 \in \mathbb{V}, m_1 \geqslant m_2\}. \tag{43}$$

According to the properties of $\mathbb{L}_c$ and $\mathbb{V}$ in Proposition 1-e and Proposition 2-a, it can be inferred that the set of hole positions on the positive half of the virtual array $\mathbb{V}$ is

$$\begin{aligned} \mathbb{H}^+ = \{&\ell_h^+ | M_1M_2d < \ell_h^+ < \\ &\max\{2(M_1-1)M_2d, 2(M_2-1)M_1d\}\}. \end{aligned} \tag{44}$$

Consider a subset of $\mathbf{\Sigma}_V$, called $\mathbf{\Sigma'}_V$, as follows

$$\begin{aligned} \mathbf{\Sigma'}_V = \{&\ell'_V | \ell'_V = m_1-m_2+1, m_1 = \Delta, \\ &0 < m_2 \leqslant M_1M_2d\}, \end{aligned} \tag{45}$$

where $\Delta = \max\{2(M_1-1)M_2d, 2(M_2-1)M_1d\}$. It is easy to obtain

$$\begin{aligned} \mathbf{\Sigma'}_V &= \{\ell'_V | \Delta - M_1M_2d+1 \leqslant \ell'_V \leqslant \Delta\} \\ &= \{\ell'_V | M_1M_2d - \min\{2M_1d, 2M_2d\}+1 \leqslant \ell'_V \leqslant \Delta\}. \end{aligned} \tag{46}$$

Combining (44-46), one can attain

$$\mathbb{H}^+ \subseteq \mathbf{\Sigma'}_V \subseteq \mathbf{\Sigma}_V. \tag{47}$$

Similarly, it can be proven that the set of hole positions $\mathbb{H}^-$ on the negative half of the virtual array is a subset of $\mathbf{\Sigma}_V$. Therefore, the virtual array $\mathbb{V}$ is a redundant array.

For better understanding, an array example is given, as shown in Fig. 2, with $M_1 = 5$ and $M_2 = 3$.

V. Performance Analysis

A. Cramér-Rao Lower Bound

At first, we analyze the Cramér-Rao Lower Bound (CRLB) and derive the closed-form expression for the 2-D angle and range parameters of near-field sources. The specific process is detailed as follows.

According to (8), the covariance matrix can be calculated as follows:

$$\mathbf{R}_c = E\{\mathbf{Z}\mathbf{Z}^H\} = \mathbf{A}_z\mathbf{P}_s\mathbf{A}_z^H + \sigma^2\mathbf{I}, \tag{48}$$

where $\mathbf{Z} = [\mathbf{z}(1), \mathbf{z}(2), \cdots, \mathbf{z}(T)]$, $\mathbf{P}_s = \mathbf{S}\mathbf{S}^H$ with $\mathbf{S} = [\mathbf{s}(1), \mathbf{s}(2), \cdots, \mathbf{s}(T)]$, and $\mathbf{I}$ is an identity matrix of dimension $2(M_1+M_2)+M_y-3$.

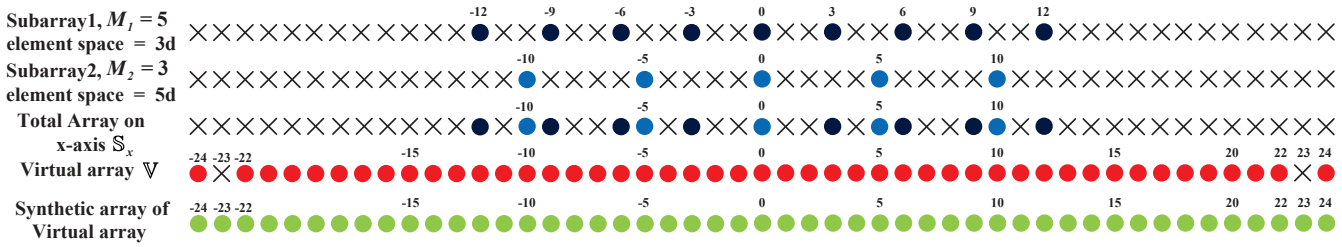

Fig. 2. An array example with $M_1 = 5$, and $M_2 = 3$.

Then, define a vector of unknown parameters as $\boldsymbol{\xi} = [\boldsymbol{\alpha}^T, \boldsymbol{\beta}^T, \mathbf{r}^T, \mathbf{p}_s^T, \sigma^2]^T$ with $\boldsymbol{\alpha} = [\alpha_1, \alpha_2, \cdots, \alpha_K]^T$, $\boldsymbol{\beta} = [\beta_1, \beta_2, \cdots, \beta_K]^T$, $\mathbf{r} = [r_1, r_2, \cdots, r_K]^T$ and $\mathbf{p}_s = [\mathbf{P}_s(1,1), \mathbf{P}_s(2,2), \cdots, \mathbf{P}_s(K,K)]$.

The CRLB is obtained by the Fisher information matrix (FIM) whose (i,j)-th element is given by [30],

$$\mathbf{FIM}_{i,j} = T\mathrm{tr}\left[\frac{\partial \mathbf{R}_c}{\partial \xi_i}\mathbf{R}_c^{-1}\frac{\partial \mathbf{R}_c}{\partial \xi_j}\mathbf{R}_c^{-1}\right], \tag{49}$$

where T denotes the number of snapshots and ξ_i denotes the i-th entry of $\boldsymbol{\xi}$. Then, by performing vectorization operation on $\mathbf{R}_c$, one can obtain

$$\mathbf{q} = vec(\mathbf{R}_c) = (\mathbf{A}_z^* \odot \mathbf{A}_z)\mathbf{p} + \sigma^2\mathbf{i}, \tag{50}$$

where $\mathbf{p} = vec(\mathbf{P})$ and $\mathbf{i} = vec(\mathbf{I})$.

Therefore, the FIM can be rewritten as

$$\mathrm{FIM} = T\left[\frac{\partial \mathbf{q}}{\partial \boldsymbol{\xi}}\right]^H (\mathbf{R}_c^T \otimes \mathbf{R}_c)^{-1}\frac{\partial \mathbf{q}}{\partial \boldsymbol{\xi}}. \tag{51}$$

According to the definition of $\boldsymbol{\xi}$, we have

$$\begin{aligned}\frac{\partial \mathbf{q}}{\partial \boldsymbol{\xi}} &= [\frac{\partial \mathbf{q}}{\partial \boldsymbol{\alpha}}, \frac{\partial \mathbf{q}}{\partial \boldsymbol{\beta}}, \frac{\partial \mathbf{q}}{\partial \mathbf{r}}, \frac{\partial \mathbf{q}}{\partial \mathbf{p}_s}, \frac{\partial \mathbf{q}}{\partial \sigma^2}] \\ &= [\mathbf{A}_z^{\boldsymbol{\alpha}}\mathbf{P}_s, \mathbf{A}_z^{\boldsymbol{\beta}}\mathbf{P}_s, \mathbf{A}_z^{\mathbf{r}}\mathbf{P}_s, \mathbf{A}_z^* \odot \mathbf{A}_z, \mathbf{i}] \\ &= [\tilde{\mathbf{A}}_z\tilde{\mathbf{P}}_s, \mathbf{A}_z^* \odot \mathbf{A}_z, \mathbf{i}],\end{aligned} \tag{52}$$

where $\tilde{\mathbf{A}}_z = [\mathbf{A}_z^{\boldsymbol{\alpha}}, \mathbf{A}_z^{\boldsymbol{\beta}}, \mathbf{A}_z^{\mathbf{r}}]$, $\tilde{\mathbf{P}}_s = \mathbf{I}_{3\times 3} \otimes \mathbf{P}_s$, in which $\mathbf{A}_z^{\boldsymbol{\alpha}} = \frac{\partial \mathbf{A}^*}{\partial \boldsymbol{\alpha}} \odot \mathbf{A} + \mathbf{A}^* \odot \frac{\partial \mathbf{A}}{\partial \boldsymbol{\alpha}}$, $\mathbf{A}_z^{\boldsymbol{\beta}} = \frac{\partial \mathbf{A}^*}{\partial \boldsymbol{\beta}} \odot \mathbf{A} + \mathbf{A}^* \odot \frac{\partial \mathbf{A}}{\partial \boldsymbol{\beta}}$, $\mathbf{A}_z^{\mathbf{r}} = \frac{\partial \mathbf{A}^*}{\partial \mathbf{r}} \odot \mathbf{A} + \mathbf{A}^* \odot \frac{\partial \mathbf{A}}{\partial \mathbf{r}}$. To obtain the CRLB of the 2-D angles and ranges, we define $\boldsymbol{\eta} = \left[\boldsymbol{\alpha}^T, \boldsymbol{\beta}^T, \mathbf{r}^T\right]$, $\boldsymbol{\gamma} = [\mathbf{p}_s^T, \sigma^2]^T$ and let

$$\begin{aligned}\mathbf{Q}_{\boldsymbol{\eta}} &= \left(\mathbf{R}^T \otimes \mathbf{R}\right)^{-\frac{1}{2}}\tilde{\mathbf{A}}_z\tilde{\mathbf{P}}_s \\ \mathbf{Q}_{\boldsymbol{\gamma}} &= \left(\mathbf{R}^T \otimes \mathbf{R}\right)^{-\frac{1}{2}}[\mathbf{A}_z^* \odot \mathbf{A}_z, \mathbf{i}].\end{aligned} \tag{53}$$

Furthermore, the FIM can be changed to

$$\mathbf{FIM} = T\begin{bmatrix}\mathbf{Q}_{\boldsymbol{\eta}}^H\mathbf{Q}_{\boldsymbol{\eta}} & \mathbf{Q}_{\boldsymbol{\eta}}^H\mathbf{Q}_{\boldsymbol{\gamma}} \\ \mathbf{Q}_{\boldsymbol{\eta}}\mathbf{Q}_{\boldsymbol{\gamma}}^H & \mathbf{Q}_{\boldsymbol{\gamma}}\mathbf{Q}_{\boldsymbol{\gamma}}^H\end{bmatrix}. \tag{54}$$

Finally, the CRLB of 2-D angles and ranges can be obtained as

$$\mathrm{CRLB}_{\boldsymbol{\eta}} = \frac{1}{T}\left(\mathbf{Q}_{\boldsymbol{\eta}}^H\boldsymbol{\Pi}_{\mathbf{Q}_{\boldsymbol{\gamma}}}^{\perp}\mathbf{Q}_{\boldsymbol{\eta}}\right)^{-1}, \tag{55}$$

where $\boldsymbol{\Pi}_{\mathbf{Q}_{\boldsymbol{\gamma}}}^{\perp} = \mathbf{I} - \mathbf{Q}_{\boldsymbol{\gamma}}(\mathbf{Q}_{\boldsymbol{\gamma}}^H\mathbf{Q}_{\boldsymbol{\gamma}})^{-1}\mathbf{Q}_{\boldsymbol{\gamma}}^H$.

B. Complexity Analysis

In this part, the complexity of the proposed algorithm and the comparison algorithms is analyzed. The complexity evaluation primarily focuses on the following components: 1) the construction of the virtual array; 2) computation of the covariance matrix; 3) Eigenvalue Decomposition (EVD); 4) spectral peak search; and 5) the optimization process. Here, define the search interval of α as $\Delta\theta_\alpha$, the search interval of β as $\Delta\theta_\beta$, and the search interval of r as Δr. Let $Ran = 2D^2/\lambda - 0.62\sqrt{(D^3/\lambda)}$ represents the search range, where D denotes array aperture, and DoF represents the degrees of freedom of the virtual array. Then, the complexity of all algorithms can be obtained, as shown in Table. I.

TABLE I
SUMMARY OF ALGORITHMS' COMPLEXITY

Methods	Complexity
Proposed	$O\{9(2(M_1+M_2)-3)^2KL + 81KL + 5DoF * L + (5DoF)^2K + K^2(5DoF)^{2.5} + 2(2(M_1+M_2)-1)L + (2(2(M_1+M_2)-1))^2L + (2(2(M_1+M_2)-1))^3(2(2(M_1+M_2)-1))^2Ran/\Delta r\}$
Wu	$O\{27(2(M_1+M_2)-3) + K^2(3(2(M_1+M_2)-3))^{2.5} + (3(2(M_1+M_2)-3))^2K + \pi(2(M_1+M_2)-1)^2/\Delta r + K^3\}$
Challa	$O\{9(2(M_1+M_2)-3)^2KL + (2(M_1+M_2)-3)^5 + 2(2(M_1+M_2)-3)^2L + (2(M_1+M_2)-3)^3 + 81KL + 18L\}$
Deng	$O\{2(2(M_1+M_2)-4)L + (2(M_1+M_2)-4)^3 + 2(2(M_1+M_2)-3)L + (2(M_1+M_2)-3)^3\}$
TSMUSIC	$O\{9(2(M_1+M_2-1)+1)^2K + 9(4(M_1+M_2-1)+1)^2K + (2(M_1+M_2-1)+1)^3 + (2(M_1+M_2-1)+1)^3 + (2(M_1+M_2-1)+1)^2\pi/\Delta\theta_\alpha + 81K + 225K + 9\pi/\Delta\theta_\beta\}$
Chen	$O\{N_xN_y(T-L+1)(2L-1) + (2N_xN_y)^2(2L-1) + 4/3(2N_xN_y)^3 + \pi N_x(N_y+1)(2N_xN_y)^2/\Delta\theta_\beta + \pi K\cdot(N_x+1)(N_y+1)^2N_x(N_xN_y)/\Delta\theta_\alpha + Ran\cdot K(2N_xN_y)^2/\Delta r\}$

VI. Simulation Results

Simulations are conducted to demonstrate the performance of the proposed method in comparison with Chen's method [28], TSMUSIC [31], Wu's algorithm [32], Challa's algorithm [33], and Deng's algorithm [34]. The impinging non-Gaussian source signals are modelled as $e^{j\varphi_t}$, where φ_t are uniformly distributed in $[0, 2\pi]$. The inter-element spacing is set to $\lambda/4$

TABLE II
RUNTIME COMPARISON.

	Proposed	TSMUSIC	Challa	Deng	Wu	Chen
Runtime(s)	17.7883	0.5439	1.4202	0.0014	1.6572	5.7863

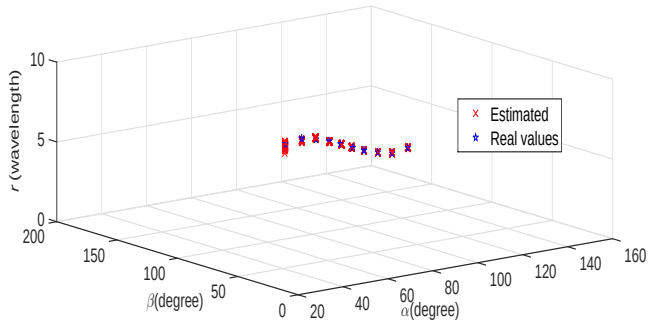

Fig. 3. 3-D scattergram of the estimated 10 NF sources.

, and the noise is assumed to be additive white Gaussian with power σ_w^2. All NF signals are of equal power σ_s^2, and the signal-to-noise ratio (SNR) is defined as $10\log_{10}\left(\sigma_s^2/\sigma_w^2\right)$. Define the estimation root-mean-square error (RMSE) from M_c Monte Carlo trials as:

$$RMSE = \sqrt{\frac{1}{M_c K}\sum_{m_c=1}^{M_c}\sum_{k=1}^{K}\left(\hat{x}_k^{(m_c)} - x_k\right)^2}. \tag{56}$$

Firstly, the underdetermined case is considered, where there are 10 narrowband NF signals parameterized by $\{(23°, 16°, 9.00\lambda), (44°, 42°, 8.2263\lambda), (59°, 58°, 7.4526\lambda), (72°, 71°, 6.6788\lambda), (84°, 84°, 5.9051\lambda), (96°, 96°, 5.1314\lambda), (108°, 109°, 4.3577\lambda), (121°, 122°, 3.5840\lambda), (136°, 138°, 2.8130\lambda), (157°, 164°, 2.0365\lambda)\}$, incident on the array with 9 elements in total ($M_1 = 2, M_2 = 3, M_y = 3$). The SNR is set to 30dB, and the total number of snapshots is 5000 with pseudo snapshots being 100. The number of Monte Carlo trials is 100. The simulation results are shown in Fig. 3, where it can be seen that the 2-D angles and range parameters of the 10 signals have been successfully identified and correctly paired, showing that the proposed method is effective for underdetermined estimation.

Secondly, the performance in terms of RMSE versus SNR is investigated, where two NF signals arrive from $\{(80°, 70°, 1.8\lambda), (130°, 140°, 2.3\lambda)\}$. Except for Challa's algorithm, the other ones have a total of 11 array elements. TSMUSIC, Deng's algorithm, and Wu's algorithm all adopt a symmetric ULA with 7 elements on the x-axis and 5 elements on the y-axis, for the proposed, we set $M_1 = 2, M_2 = 3, M_y = 5$. Challa's algorithm requires an even number of elements along both axes, so in the simulation, it employs a ULA with 8 elements on the x-axis and 6 elements on the y-axis. The total number of snapshots is 1100, the number of pseudo snapshots of the proposed algorithm, Deng's algorithm, and Challa's algorithm is all set to 100, and the SNR varies from 0dB to 30dB. The results are shown in Fig. 4.

It can be observed that the estimation performance of the proposed algorithm for both angle α and range parameters is significantly better than the compared algorithms. For angle β, the proposed algorithm is better than Deng's algorithm, and is similar to Challa's algorithm, Wu's algorithm and TSMUSIC, but slightly worse than Chen's algorithm. This is because the proposed algorithm generates $2M-1$ virtual elements along the y-axis, one less than the $2M$ virtual elements generated by the Chen's algorithm. This difference accounts for the slightly superior performance observed with Chen's algorithm, as the extra virtual element enhances its estimation capability. In addition, it should be noted that, for the estimation of β, Chen's method is found to tightly follow the CRLB or even coincident. This is because, in this paper, we derive CRLB based on coarray for the considered nonuniform cross array, while Chen's method uses uniform cross arrays. Thus, the derived CRLB is not the benchmark for Chen's method.

In the third part, the influence of the number of snapshots on estimation performance is studied. Except for the number of snapshots and SNR, the other parameters are consistent with the second simulation. Here, SNR = 5dB, and the number of snapshots varies from 200 to 5000. The results are shown in Fig. 5. It can be observed that for the first angle parameter α and range parameter, the proposed algorithm outperforms all the others, while for the second angle parameter β, the proposed algorithm is superior to Deng's algorithm, Wu's algorithm and TSMUSIC, and is similar to Challa's algorithm, but slightly worse than Chen's algorithm.

In the fourth part, the influence of range separation on estimation performance is studied. The parameter settings are the same as the second simulation, except that the SNR is fixed at 5dB, the initial range of the second source becomes the same as the first one, and the range separation $\Delta\lambda$ of the second source varies from 0 to 1.3λ. The results are shown in Fig. 6. It can be found that for 2-D angle parameters, the increase of range separation has a little influence on estimation performance. For range item, the estimation performance declines as the range separation increases. In addition, the proposed algorithm is superior to other comparison algorithms in terms of α and range parameters. However, for β, it performs slightly worse than Chen's algorithm.

In the fifth part, the runtime comparison of all algorithms is examined. The parameter settings are same as the second simulation, except that the SNR is fixed at 20dB and the number of snapshots is 2000. The results are shown in Table. II. It can be found that the runtime of the proposed algorithm is slightly higher than that of other comparison algorithms. This is mainly because the proposed algorithm involves high-

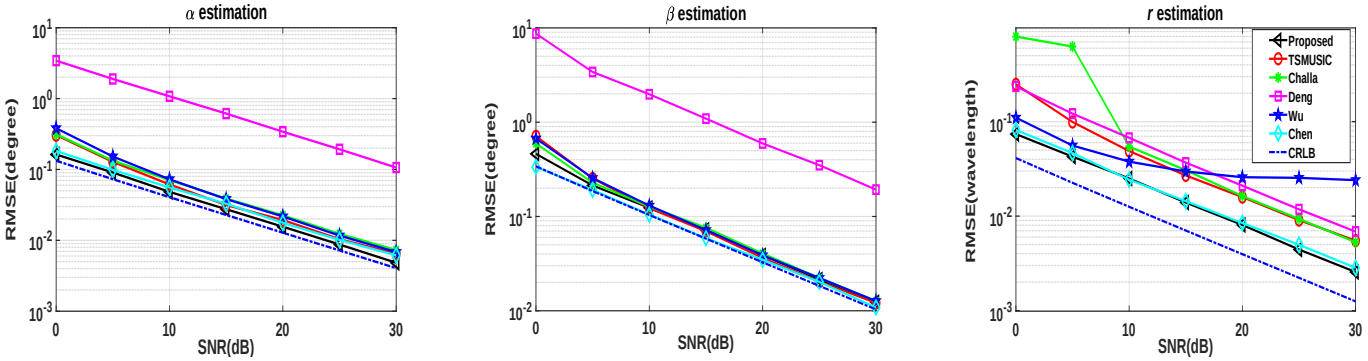

(a) RMSE-α (b) RMSE-β (c) RMSE-r

Fig. 4. RMSE versus SNR.

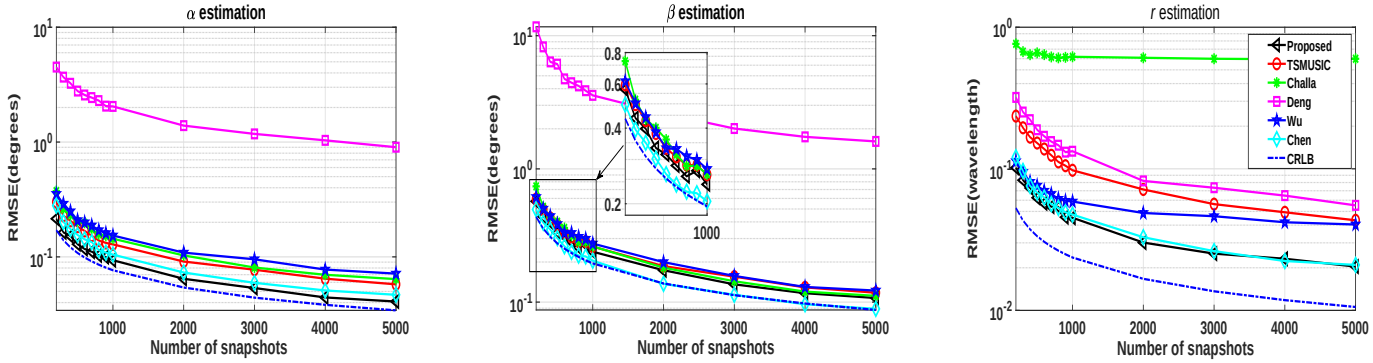

(a) RMSE-α (b) RMSE-β (c) RMSE-r

Fig. 5. RMSE versus the number of snapshots.

order cumulants construction, optimization operations for angle solution and spectral peak search procedures. Although having higher complexity, the proposed method has superior estimation performance to the other methods.

Finally, we consider the scenario with mixed N-F and FF sources. Except for the interested parameters of the incoming sources, all other configuration parameters are the same as the first simulation. In this part, the number of near-field sources is set to 7, with parameters $\{(72°, 72°, 9.0000\lambda), (84°, 84°, 7.8394\lambda), (96°, 96°, 6.6788\lambda), (108°, 108°, 5.5183\lambda), (121°, 121°, 4.3577\lambda), (136°, 136°, 3.1971\lambda), (157°, 157°, 2.0365\lambda)\}$; the number of far-field sources is set to 3, with parameters $\{(23°, 23°), (44°, 44°), (59°, 59°)\}$. The results are shown in Fig. 7. Clearly, the angles of all 10 mixed sources have been correctly identified. Additionally, Fig. 7(b) demonstrates that the ranges of near-field sources have also been effectively estimated. Furthermore, all the mentioned parameters are correctly paired. So the proposed algorithm can still work in the mixed source scenario.

VII. Conclusion

A near-field 3-D parameter estimation algorithm based on a symmetric nonuniform cross array has been proposed, which fully utilizes the spatial-temporal information of the received signals. With FOC, the virtual array data is constructed that is equivalent to far-field pseudo observations. Then, SPA and two-level Toeplitz matrix decomposition techniques are introduced to achieve estimation of 2-D angles with increased DOFs in the virtual array. Finally, by exploiting the conjugate symmetry property of the signal's autocorrelation function, another set of virtual array data containing the range parameters is generated, and the range parameters are estimated using the 1-D MUSIC algorithm. As demonstrated by simulation results, the proposed algorithm can achieve underdetermined 3-D parameter estimation that is automatically paired, and it outperforms four representative existing algorithms.

References

[1] W. Liu, M. Haardt, M. S. Greco, C. F. Mecklenbrauker, and P. Willett, "Twenty-five years of sensor array and multichannel signal processing: A review of progress to date and potential research directions," *IEEE Signal Processing Magazine*, vol. 40, no. 4, pp. 80–91, 2023.

[2] A. M. Elbir and K. V. Mishra, "Sparse array selection across arbitrary sensor geometries with deep transfer learning," *IEEE Transactions on Cognitive Communications and Networking*, vol. 7, no. 1, pp. 255–264, 2021.

[3] H. Chen, W. Wang, W. Liu, Y. Tian, and G. Wang, "An exact near-field model based localization for bistatic MIMO radar with COLD arrays," *IEEE Transactions on Vehicular Technology*, pp. 1–10, 2023.

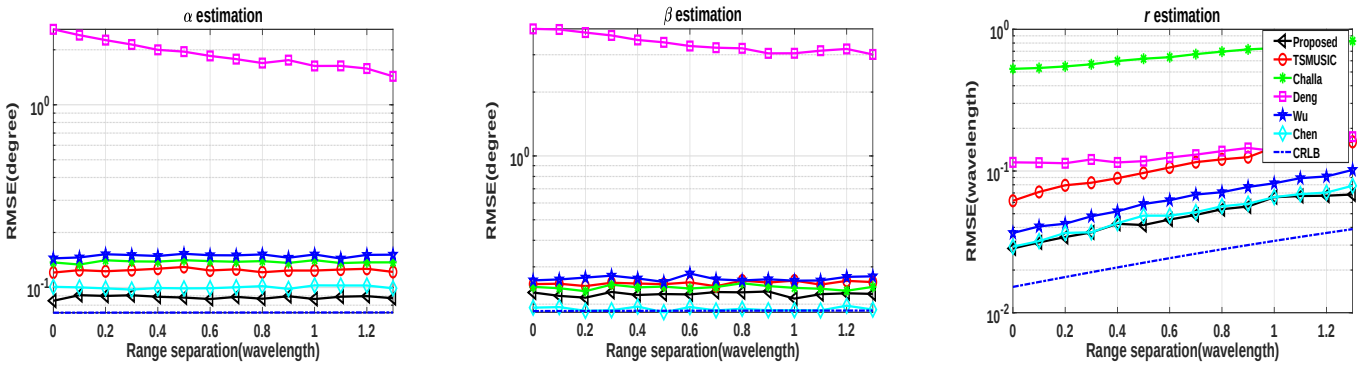

(a) RMSE-α (b) RMSE-β (c) RMSE-r

Fig. 6. RMSE versus range separation.

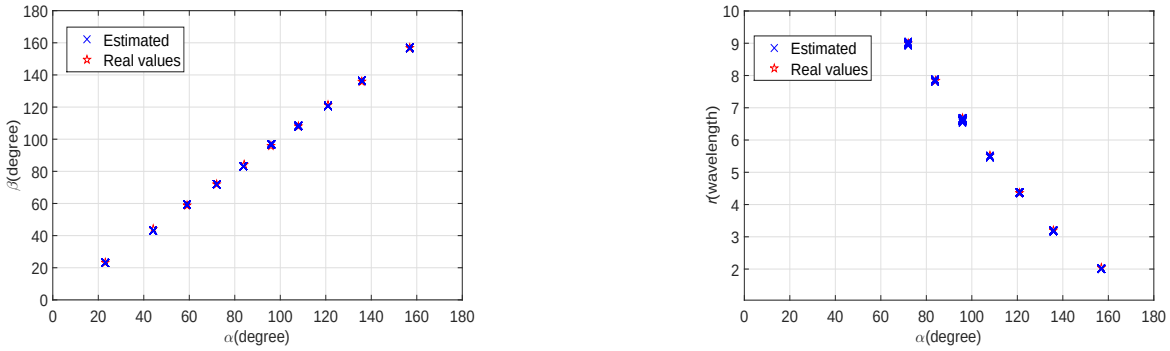

(a) Estimation results of 2-D angles. (b) Estimation results of angle α and range.

Fig. 7. Estimation results under a mixed-source scenario.

[4] A. M. Elbir and T. E. Tuncer, "Far-field DOA estimation and near-field localization for multipath signals," *Radio Science*, vol. 49, no. 9, pp. 765–776, 2014.

[5] J. Shi, F. Wen, and T. Liu, "Nested MIMO radar: Coarrays, tensor modeling, and angle estimation," *IEEE Transactions on Aerospace and Electronic Systems*, vol. 57, no. 1, pp. 573–585, 2021.

[6] T. Shu, J. He, F. Wen, and T.-K. Truong, "Incompletely polarized mimo radar for target direction estimation," *IEEE Transactions on Radar Systems*, vol. 1, pp. 532–541, 2023.

[7] F. Wen, G. Gui, H. Gacanin, and H. Sari, "Compressive sampling framework for 2D-DOA and polarization estimation in mmwave polarized massive MIMO systems," *IEEE Transactions on Wireless Communications*, vol. 22, no. 5, pp. 3071–3083, 2023.

[8] A. M. Molaei, B. Zakeri, and S. M. Hosseini Andargoli, "Components separation algorithm for localization and classification of mixed near-field and far-field sources in multipath propagation," *IEEE Transactions on Signal Processing*, vol. 68, pp. 404–419, 2020.

[9] J. Li, Y. Wang, Z. Ren, X. Gu, M. Yin, and Z. Wu, "DOA and range estimation using a uniform linear antenna array without a priori knowledge of the source number," *IEEE Transactions on Antennas and Propagation*, vol. 69, no. 5, pp. 2929–2939, 2021.

[10] W. Zuo, J. Xin, N. Zheng, H. Ohmori, and A. Sano, "Subspace-based near-field source localization in unknown spatially nonuniform noise environment," *IEEE Transactions on Signal Processing*, vol. 68, pp. 4713–4726, 2020.

[11] W. Zuo, J. Xin, W. Liu, N. Zheng, H. Ohmori, and A. Sano, "Localization of near-field sources based on linear prediction and oblique projection operator," *IEEE Transactions on Signal Processing*, vol. 67, no. 2, pp. 415–430, 2019.

[12] B. Wang, Y. Zhao, and J. Liu, "Mixed-order MUSIC algorithm for localization of far-field and near-field sources," *IEEE Signal Processing Letters*, vol. 20, no. 4, pp. 311–314, 2013.

[13] Z. Zheng, M. Fu, W.-Q. Wang, S. Zhang, and Y. Liao, "Localization of mixed near-field and far-field sources using symmetric double-nested arrays," *IEEE Transactions on Antennas and Propagation*, vol. 67, no. 11, pp. 7059–7070, 2019.

[14] Y. Tian, Q. Lian, and H. Xu, "Mixed near-field and far-field source localization utilizing symmetric nested array," *Digital Signal Processing*, vol. 73, pp. 16–23, 2018.

[15] J. Zhang, Y. Li, J. Qi, and Y. Li, "Symmetric extended nested array for passive localization of mixture near- and far-field sources," *IEEE Transactions on Circuits and Systems II: Express Briefs*, vol. 70, no. 3, pp. 1244–1248, 2023.

[16] H. Yan, Y. Wang, Y. Gong, Z. Zhang, and L. Wang, "Improved sparse symmetric arrays design for mixed near-field and far-field source localization," *IEEE Transactions on Aerospace and Electronic Systems*, pp. 1–12, 2023.

[17] X. Su, P. Hu, Z. Liu, T. Liu, B. Peng, and X. Li, "Mixed near-field and far-field source localization based on convolution neural networks via symmetric nested array," *IEEE Transactions on Vehicular Technology*, vol. 70, no. 8, pp. 7908–7920, 2021.

[18] Z. Zheng, M. Fu, W.-Q. Wang, and H. C. So, "Symmetric displaced coprime array configurations for mixed near- and far-field source localization," *IEEE Transactions on Antennas and Propagation*, vol. 69, no. 1, pp. 465–477, 2021.

[19] X. Wu, W.-P. Zhu, and J. Yan, "Atomic norm based localization of far-field and near-field signals with generalized symmetric arrays," in *ICASSP 2020 - 2020 IEEE International Conference on Acoustics, Speech and Signal Processing (ICASSP)*, 2020, pp. 4762–4766.

[20] J. He, L. Li, T. Shu, and T.-K. Truong, "Mixed near-field and far-field source localization based on exact spatial propagation geometry," *IEEE Transactions on Vehicular Technology*, vol. 70, no. 4, pp. 3540–3551, 2021.

[21] J. He, T. Shu, L. Li, and T.-K. Truong, "Mixed near-field and far-field localization and array calibration with partly calibrated arrays," *IEEE Transactions on Signal Processing*, vol. 70, pp. 2105–2118, 2022.

[22] X. Wu and W.-P. Zhu, "Single far-field or near-field source localization with sparse or uniform cross array," *IEEE Transactions on Vehicular Technology*, vol. 69, no. 8, pp. 9135–9139, 2020.

[23] X. Wu, "Localization of far-field and near-field signals with mixed sparse approach: A generalized symmetric arrays perspective," *Signal Processing*, vol. 175, p. 107665, 2020.

[24] Z. Yang, L. Xie, and C. Zhang, "A discretization-free sparse and parametric approach for linear array signal processing," *IEEE Transactions on Signal Processing*, vol. 62, no. 19, pp. 4959–4973, 2014.

[25] Z. Yang, L. Xie, and P. Stoica, "Vandermonde decomposition of multilevel toeplitz matrices with application to multidimensional super-resolution," *IEEE Transactions on Information Theory*, vol. 62, no. 6, pp. 3685–3701, 2016.

[26] H. Chen, W. Wang, and W. Liu, "Joint DOA, range, and polarization estimation for rectilinear sources with a cold array," *IEEE Wireless Communications Letters*, vol. 8, no. 5, pp. 1398–1401, 2019.

[27] Y. Cao, T. Lv, Z. Lin, P. Huang, and F. Lin, "Complex resnet aided DoA estimation for near-field MIMO systems," *IEEE Transactions on Vehicular Technology*, vol. 69, no. 10, pp. 11 139–11 151, 2020.

[28] H. Chen, Z. Jiang, W. Liu, Y. Tian, and G. Wang, "Conjugate augmented decoupled 3-D parameters estimation method for near-field sources," *IEEE Transactions on Aerospace and Electronic Systems*, vol. 58, no. 5, pp. 4681–4689, 2022.

[29] P. P. Vaidyanathan and P. Pal, "Sparse sensing with co-prime samplers and arrays," *IEEE Transactions on Signal Processing*, vol. 59, no. 2, pp. 573–586, 2011.

[30] M. Wang and A. Nehorai, "Coarrays, music, and the cramrcrao bound," *IEEE Transactions on Signal Processing*, vol. 65, no. 4, pp. 933–946, 2017.

[31] J. Liang and D. Liu, "Passive localization of mixed near-field and far-field sources using two-stage MUSIC algorithm," *IEEE Transactions on Signal Processing*, vol. 58, no. 1, pp. 108–120, 2010.

[32] X. Wu and J. Yan, "3-D mixed far-field and near-field sources localization with cross array," *IEEE Transactions on Vehicular Technology*, vol. 69, no. 6, pp. 6833–6837, 2020.

[33] R. N. Challa and S. Shamsunder, "Passive near-field localization of multiple non-gaussian sources in 3-D using cumulants," *Signal Processing*, vol. 65, no. 1, pp. 39–53, 1998.

[34] K. Deng and Q. Yin, "Closed form parameters estimation for 3-D near field sources," in *2006 IEEE International Conference on Acoustics Speech and Signal Processing Proceedings*, vol. 4, 2006, pp. IV–IV.